



ISTITUTO NAZIONALE DI RICERCA METROLOGICA Repository Istituzionale

Exact formulation for hysteresis loops and energy loss in Stoner-Wohlfarth systems

Original

Exact formulation for hysteresis loops and energy loss in Stoner-Wohlfarth systems / Appino, C.. - In: AIP ADVANCES. - ISSN 2158-3226. - 13:(2023), pp. 055018-1-055018-12. [10.1063/5.0143905]

Availability:

This version is available at: 11696/79520 since: 2025-01-23T09:05:19Z

Publisher:

American Institute of Physics

Published

DOI:10.1063/5.0143905

Terms of use:

This article is made available under terms and conditions as specified in the corresponding bibliographic description in the repository

Publisher copyright

(Article begins on next page)

Exact formulation for hysteresis loops and energy loss in Stoner–Wohlfarth systems

Cite as: AIP Advances 13, 055018 (2023); doi: 10.1063/5.0143905

Submitted: 6 March 2023 • Accepted: 17 April 2023 •

Published Online: 16 May 2023



View Online



Export Citation



CrossMark

C. Appino^{a)}

AFFILIATIONS

Istituto Nazionale di Ricerca Metrologica (INRIM), Strada delle Cacce 91, 10135 Torino, Italy

^{a)}Author to whom correspondence should be addressed: c.appino@inrim.it

ABSTRACT

We propose an exact expression to describe the hysteresis loops of an ensemble of Stoner–Wohlfarth particles undergoing an alternating quasi-static magnetic field. A statistical approach, which treats the quantities characterizing each particle as random variables, is adopted to get the orientation distribution of the local polarizations with respect to the applied field direction and the constitutive equation of the whole particle assembly. The hysteresis loop area gives the energy loss figure, but we have also obtained a straightforward integral expression for this quantity. The analytical relationships for the symmetric loops and the losses are successfully tested against numerical results, and the mathematical method adopted also displayed the ability to reproduce the “elemental loop” associated with any given particle of the system. While having a fundamental character, the proposed approach bears applicative interest, representing a versatile tool as the core of codes that simulate the behavior of devices employing magnetic components.

© 2023 Author(s). All article content, except where otherwise noted, is licensed under a Creative Commons Attribution (CC BY) license (<http://creativecommons.org/licenses/by/4.0/>). <https://doi.org/10.1063/5.0143905>

I. INTRODUCTION

Magnetic materials exhibit a broad variety of compositions and microstructures and a wide spectrum of responses to a varying magnetizing field \vec{H} .^{1–3}

Although such behavior is the result of three-dimensional (3D) magnetization process, a two-dimensional theoretical approach is often regarded as appropriate, in addition to being perfectly adequate for a large class of materials, such as steel sheets, amorphous and nanocrystalline alloys, and thin films. It is also possible, in many cases, to consider a given material as an ensemble of mesoscopic regions (“particles”), either interacting or independent, each characterized by the local polarization \vec{J}_s and a magnetic anisotropy {uniaxial [see Fig. 1(a)], biaxial, cubic, etc.}, and even single-domain, if sufficiently small.

The Stoner–Wohlfarth (SW) theory,^{4–8} in its native formulation (which considers single-domain particles as independent, endowed with uniaxial anisotropy, and at $T = 0$ K), fits the simplifications mentioned above and is, thus, widely exploited in modeling. The main fields where the SW approach (often with some modifications) plays an important role are (1) magnetic nanoparticles,^{9–12} notably for magnetic hyperthermia;^{13,14} (2) ferromagnetic thin films^{15–17} and magnetic random access memories;^{18–20}

(3) amorphous and nanocrystalline materials;^{21–25} (4) soft magnetic composites;^{26,27} (5) permanent magnets;²⁸ and (6) study of the effect of spin-polarized currents.^{29,30}

In the SW model, the response to an applied field \vec{H} of a particle characterized by the local uniaxial anisotropy \vec{K} is described by a vector hysteresis transducer providing the constitutive law for the reversible coherent rotations and the irreversible jumps of the local polarization \vec{J}_s . In other words, one gets the equilibrium orientation γ of each \vec{J}_s as a function of the anisotropy constant K , its orientation φ , and \vec{H} [see Fig. 1(a)]. With \vec{J} being the polarization of the whole particle assembly, the $\vec{J}(\vec{H})$ constitutive equation of the system comes out after integration over the probability density functions (pdfs) of K and φ . The design of magnetic components needs to implement $\vec{J}(\vec{H})$ in numeric modeling codes: a step with high computational cost, scaling up with the device size. Indeed, an explicit $\gamma = \gamma_H(K, \varphi)$ solution for the \vec{J}_s orientation is not available so far, being the equilibrium angle obtained either following numeric procedures^{25,31} or using analytic approximations.

In the first case, the problem is commonly faced by adopting the astroid representation for the SW transducer [see Fig. 1(b)] and exploiting the so-called “tangent method,”⁷ as well as searching for the minimum of the Gibbs free energy of each particle

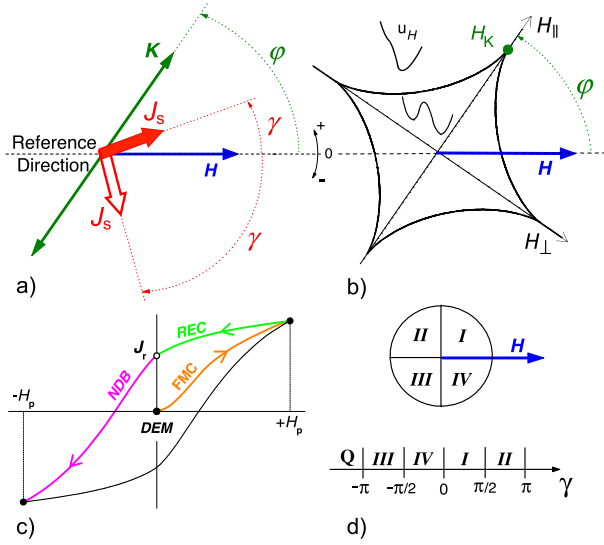


FIG. 1. Panel (a) shows, for a particle of the system, the relative orientation of the local anisotropy \vec{K} and the local polarization \vec{J}_s with respect to the reference direction determined by the applied field \vec{H} . In the $(H_{\parallel}, H_{\perp})$ plane, the corresponding astroid representation, with vertices $\pm H_K$, is displayed in (b), with u_H being the associated Gibbs free energy. (c) Branches of a general hysteresis loop, drawn starting from the demagnetized state (DEM). (d) Correspondence between the Q quadrants and the values of the γ angle.

utilizing, e.g., the Newton–Raphson method. These are time-consuming approaches, not efficient when implemented in codes used to design magnetic devices.

Researchers following the second way tried, for example, to recover the SW loop branches with *ad hoc* analytic functions,³² or proposed an $H = H(J)$ “inverse” constitutive law,¹² or limited the analytic solution to the low-field regime.³³ Alternatively, an SW-like hysteron with different kinds of approximations for the anisotropy energy term,^{34,35} or with an equivalent field playing the role of the anisotropy,³⁶ has been also adopted.

This work is not focused on the search of the $\gamma = \gamma_H(K, \varphi)$ single particle solution [see Fig. 1(a)], afterward integrated over the whole system, but it deals at the start from the entire particle assembly by handling each quantity as a random variable (rv) with associated pdf. Statistical methods^{37,38} are then utilized to retrieve $p_H(\gamma)$: the equilibrium angle pdf, ending with an exact expression for the hysteresis loops (and consequently for the energy losses) of the whole system. The single particle behavior comes out as a particular case. Apart from its importance from the basic viewpoint, this result turns out to be useful for applications (chiefly in the magnetic loss prediction³⁹), shortening the cumbersome and slow procedure needed for the design of devices.

In this paper, after a review of the SW model features essential for our purposes (Sec. II A), and some hints about the numerical approach and the adopted statistics (Sec. II B), the core of the work is discussed in Sec. III. Here, the statistical approach is outlined, and the pdfs controlling the equilibrium orientation of the local polarization vs a quasi-static \vec{H} are worked out, separately accounting

for the irreversible (Sec. III A) and reversible (Sec. III B) phenomena. In both these subsections, the pdf evolution is described starting from the demagnetized state and following the system magnetization along the branches of the hysteresis loop driven by an alternating field [Fig. 1(c)], separately for the four Q quadrants shown in Fig. 1(d). Eventually, the obtained *constitutive equation* (and thus the hysteresis loop and loss) is successfully tested against the numerical procedure, both for the entire assembly (Sec. III B 5) and for the case of a single particle (Sec. III B 6). An approximate analytic expression for the energy loss, not involving the knowledge of the hysteresis loop, is worked out and effectively checked (Sec. IV), and finally, in Sec. V, some possible advancements of the proposed approach are listed.

II. THE CLASSICAL SW MODEL AND ITS NUMERICAL IMPLEMENTATION

A. The Stoner–Wohlfarth model

The SW approach considers the physical system as an ensemble of non-interacting single-domain “particles” at $T = 0$ K, each characterized by a local anisotropy axis with modulus K (and anisotropy field $H_K = 2K/J_s$, where $J_s = |\vec{J}_s|$), forming an angle φ with a reference direction defined by the applied field \vec{H} [Fig. 1(a)]. After introducing the Gibbs free energy density of the particle, together with its first and second derivative (where $H = |\vec{H}|$),

$$u_H(K, \varphi; \gamma) = K \sin^2(\varphi - \gamma) - H J_s \cos \gamma, \quad (1a)$$

$$u'_H := \frac{\partial u_H}{\partial \gamma} = -K \sin(2\varphi - 2\gamma) + H J_s \sin \gamma, \quad (1b)$$

$$u''_H := \frac{\partial u'_H}{\partial \gamma} = 2K \cos(2\varphi - 2\gamma) + H J_s \cos \gamma, \quad (1c)$$

the γ equilibrium orientations of the local polarization \vec{J}_s (corresponding to the minima of u_H) are derived.^{4–7} This can be done starting from the conditions $u'_H = u''_H = 0$ (identifying the u_H horizontal inflection point generated by the merging of one minimum and one maximum), which allows one to draw, in the $(H_{\parallel} := H \cos \varphi, H_{\perp} := H \sin \varphi)$ Cartesian reference frame, a closed curve (astroid) whose contour (with vertices $\pm H_K$) represents the border separating the $(H_{\parallel}, H_{\perp})$ plane region corresponding to two minima of u_H (inside) from the one where one minimum only appears [Fig. 1(b)]. On passing to the polar coordinates (φ, H) , after defining the quantity

$$A(\varphi) = (\sin^{2/3} \varphi + \cos^{2/3} \varphi)^{3/2}, \quad (2)$$

the field threshold corresponding to the astroid is written as

$$H_{c,K}(\varphi) = H_K / A(\varphi). \quad (3)$$

If H is instead given, in the (φ, K) plane, where each point represents a particle of the system, one finds the corresponding always positive anisotropy threshold,

$$K_{c,H}(\varphi) = \frac{1}{2} |H| J_s A(\varphi), \quad (4)$$

with one (two) minimum (minima) when K is lower (higher) than K_{cH} .

The introduction reports the strategies followed in the literature to find the γ equilibrium angle for each particle. In the following, the statistics of the system is described by the $\psi(K, \varphi)$ joint probability density function, with $K > 0$ and φ limited to the $[0; \pi/2]$ range for symmetry reasons.

B. Numerical implementation

The numerical approach adopted in this work to test the analytic form of $J(H)$, worked out in the following, finds the local \tilde{J}_s equilibrium orientations via an iterative procedure searching for the u_H absolute minimum and follows its time evolution by tracking the memory of the irreversible rotations (IRs), for each particle. On passing to an assembly of SW particles, one gets the behavior of the whole system after integration over the $\psi(K, \varphi)$ pdf. When we compare the analytic expressions for the hysteresis loop and loss to the numerical simulations, φ and K are assumed to be statistically independent variables. Consequently, we can write $\psi(K, \varphi) = f(K)g(\varphi)$, and in particular, we have chosen for the tests, with $\langle K \rangle$ the average anisotropy value,

$$f(K) = \left(\frac{2}{\langle K \rangle} \right)^2 K \exp \left(-\frac{2}{\langle K \rangle} K \right), \quad (5a)$$

$$g(\varphi) = 2/\pi. \quad (5b)$$

III. THE ANALYTIC-STATISTICAL APPROACH FOR AN ENSEMBLE OF SW PARTICLES

In this work, we have abandoned the problem of finding the exact analytical solution for the local \tilde{J}_s equilibrium orientation γ of a single SW particle in favor of a statistical approach that considers the whole assembly of SW particles from the beginning. Accordingly, the quantities K , φ , and γ ($-\pi$ to $+\pi$) are treated as *random variables*, along with their $\psi(K, \varphi)$ and $p_H^{(b,Q)}(\gamma)$ pdfs (the first normalized to 1 for each φ angle). In the latter, “ b ” indicates the loop branch considered [see Fig. 1(c)], “ Q ” is the quadrant to which γ pertains [see Fig. 1(d)], and H plays the role of a parameter. All along the paper, the evolution of the γ values, which are bound to increase from $-\pi$ to π [see Fig. 1(d)], dictates the sequence adopted to discuss the Q quadrants ($III \rightarrow IV \rightarrow I \rightarrow II$).

As a response to an alternating field, with peak values $\pm H_p$, the corresponding hysteresis loop is obtained as follows: The magnetization process is assumed to start from the demagnetized state (DEM), where $H = J = 0$ [Fig. 1(c)]—a situation that, for symmetry reasons, can be obtained by formulating the pdf for the \tilde{J}_s equilibrium orientation still in terms of K and φ instead of γ , the local polarization lying along the easy axis direction in each particle,

$$p_{DEM}^{(Q=I)}(K, \varphi) = p_{DEM}^{(Q=III)}(K, \varphi) = \frac{1}{2} \psi(K, \varphi), \quad (6a)$$

$$p_{DEM}^{(Q=II)}(K, \varphi) = p_{DEM}^{(Q=IV)}(K, \varphi) = 0. \quad (6b)$$

[An example, for a given $\varphi = \varphi_1$ and a postulated $\psi(K, \varphi_1)$ vs K behavior, is reported in Fig. 3(a).] The J vs H evolution is then followed and investigated in sequence [see Fig. 1(c)] along the First

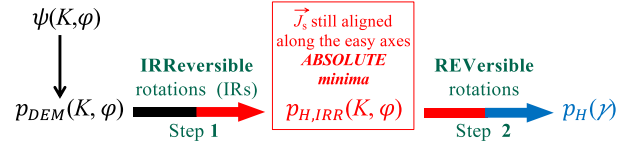


FIG. 2. Evolution of the probability density function, from the K and φ statistics to the γ statistics. The two steps describing the irreversible and reversible processes in sequence are put in evidence. The superscripts (b, Q) of the pdfs are understood for the sake of simplicity. Note the dependence on (K, φ) of p_{DEM} and $p_{H,IRR}$, and on γ of the final p_H pdf.

Magnetization Curve (FMC), the RECoil curve (REC), and the Negative Descending Branch (NDB) of the hysteresis loop, both in Secs. III A and III B. Note that the ascending branch (\uparrow) of the major loop of vertex (H_p, J_p) can be obtained from the descending one (\downarrow), build-up of the REC and NDB curves, being $J_\uparrow(H) = -J_\downarrow(-H)$ for symmetry reasons.

Along each loop branch, the applied field triggers the irreversible rotations (IRs) and drives any local \tilde{J}_s of the whole particle ensemble to its equilibrium angle (reversible rotations) at the same time. Despite the ensuing complex interplay between reversible and irreversible processes, the technique developed here treats them separately, and the γ pdf is consequently worked out in two steps: before finding $p_{H,IRR}^{(b,Q)}(K, \varphi)$, i.e., the pdf determined by the IRs only, which bring the local \tilde{J}_s to their *absolute minimum* (Sec. III A), and subsequently accounting for the coherent reversible rotations (by means of the \tilde{J}_s relaxation to the *equilibrium orientation*), ending with $p_H^{(b,Q)}(\gamma)$ (Sec. III B). This approach is sketched in Fig. 2.

Eventually, after the integration of $p_H^{(b,Q)}(\gamma) \cos \gamma$ over the $[-\pi; +\pi]$ γ domain, one gets the constitutive law of the system [Sec. III B 5, Eq. (28)].

A. Step 1: Irreversible rotations (IRs)

At this stage, we assume \vec{H} to drive the irreversible processes only, again leaving the local \tilde{J}_s to point along one of the two sides of the φ easy axis directions of the particle to which it pertains. For this reason, the magnetization distribution among the quadrants, rearranged by the occurrence of the IRs, is again described by a pdf stated in terms of K and φ instead of γ : $p_{H,IRR}^{(b,Q)}(K, \varphi)$, for the three loop branches of Fig. 1(c), as listed in Sections III A 1–III A 4, and illustrated in Fig. 3 for a given $\varphi = \varphi_1$.

1. First magnetization curve (FMC)

For H increasing from DEM [Fig. 1(c)], Eqs. (1b) and (1c) state that the \tilde{J}_s in quadrant III smoothly (i.e., without IRs) crosses the $\gamma = -\pi/2$ threshold and move to quadrant IV when $\varphi > \pi/4$ and $H > H_{III \rightarrow IV} = (K/J_s) \sin 2\varphi$ [a value always lower or equal to $H_{cK}(\varphi)$: the threshold for IRs]. As stated above, we are not interested at this stage in the equilibrium position of \tilde{J}_s , so we account for these \tilde{J}_s reversible rotations by assigning the same pdfs to these quadrants: $p_{H,IRR}^{(FMC,IV)} = p_{H,IRR}^{(FMC,III)}$. Note that this “doubling” of the $p_{H,IRR}^{(FMC,Q)}$ does not affect the normalization because each \tilde{J}_s does not pertain to $Q = III$ and $Q = IV$ for the same field, the Step 2 (Sec. III B) taking charge of finding the actual \tilde{J}_s orientation vs H . As H increases

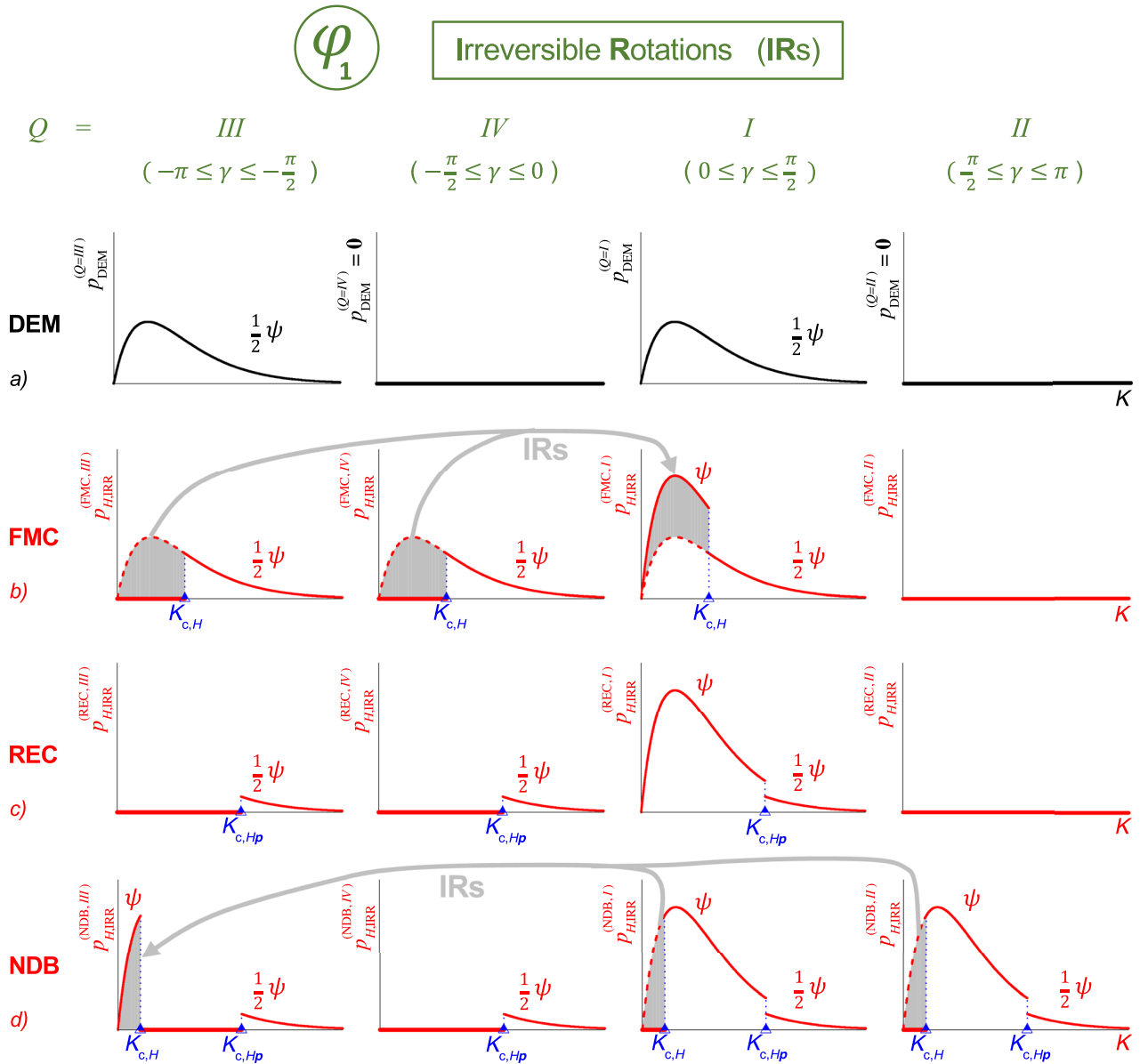


FIG. 3. For a given $\varphi = \varphi_1$, and with a postulated $\psi(K, \varphi_1)$, the evolution of the pdfs (see the left part of Fig. 2) is described for the four Q quadrants [see Fig. 1(d)]. As H drives the system along the branch sequence of Fig. 1(c), the $p_{\text{DEM}}^{(O)}$ [Eq. (6)] describing the demagnetized state (DEM) transforms into the $p_{H,\text{IRR}}^{(FMC,Q)}$, $p_{H,\text{IRR}}^{(REC,Q)}$, and $p_{H,\text{IRR}}^{(NDB,Q)}$ as a response to the irreversible rotations (IRs) displayed by the gray arrows.

from zero [where $K_{c,0} = 0$, see Eq. (4)] to the peak value H_p , the \vec{J}_s in quadrant III or IV switch to quadrant I if $K < K_{c,H}(\varphi)$, and the corresponding $p_{H,\text{IRR}}^{(FMC,Q)}(K, \varphi)$ is reported in Fig. 3(b). Note that $p_{H,\text{IRR}}^{(FMC,II)} = 0$ because the system geometry [Fig. 1(a)] does not allow irreversible rotations to the second quadrant, a fact in agreement with the detailed discussion reported in the Appendix, which shows that no energy minima of u_H [Eq. (1a)] can appear in $Q = II$.

2. Recoil curve (REC)

When the field is reduced from H_p to zero, the polarization decreases from its peak value $J_p = J(H_p)$ to the remanence J_r . Along this branch, no IRs occur, and thus, $p_{H,\text{IRR}}^{(REC,Q)}(K, \varphi)$ is frozen to the value reached along FMC at $H = H_p$: $p_{H_p,\text{IRR}}^{(FMC,Q)}(K, \varphi)$ [see Fig. 3(c)]. Here, again, we have $p_{H,\text{IRR}}^{(REC,IV)} = p_{H,\text{IRR}}^{(REC,III)}$ because the “doubling” of

the pdfs, pointed out in FMC persists, but, as above, it does not affect the normalization.

3. Negative descending branch (NDB)

Eventually, the system is brought from the remanence to the negative tip of the hysteresis loop, lowering H from 0 to $-H_p$, with the magnetization evolving as described by $p_{H,IRR}^{(NDB,Q)}(K, \varphi)$ [Fig. 3(d)]. For what concern the IRs and the smooth \tilde{f}_s transitions discussed in Sec. III A 1, a “symmetrical” reasoning applies here, with the quadrants I, II, and IV correspondingly playing the role of Q = III, IV, and I in FMC, and the $\gamma = \pi/2$ crossing occurring at the threshold $H_{I \rightarrow II} = -H_{III \rightarrow IV} \leq H_{c,K}(\varphi)$, when $\varphi > \pi/4$.

4. Thresholds of the $p_{H,IRR}^{(b,Q)}(K, \varphi)$ functions

The quantities $K_{c,H}(\varphi_1)$ and $K_{c,Hp}(\varphi_1)$ of Fig. 3, signaling a variation of the $p_{H,IRR}^{(b,Q)}$ values for a given $\varphi = \varphi_1$, become the $K_{c,H}(\varphi)$ and $K_{c,Hp}(\varphi)$ threshold functions when considering the entire $0 \leq \varphi \leq \pi/2$ range. As H , starting from the demagnetized state (DEM), oscillates between the $\pm H_p$ peak values of the hysteresis loop, the $K_{c,H}(\varphi)$ threshold follows it, swinging between $K_{c,0} = 0$ and $K_{c,Hp}(\varphi)$, with the $p_{H,IRR}^{(b,Q)}(K, \varphi)$ function that accordingly changes. An example for $Q = I$ across NDB is depicted in the (φ, K) plane of Fig. 4.

B. Step 2: Coherent reversible rotations and constitutive equation

Given H and γ , and considering the scheme of Fig. 2, for the three branches of the hysteresis loop indicated in Fig. 1(c), the $p_H^{(b,Q)}(\gamma)$ pdf, which accounts for irreversible and reversible processes, is obtained through standard statistical methods.^{37,38}

One starts by computing the cumulative distribution function $P_H^{(b,Q)}(\gamma)$, i.e., the probability for a general γ' to satisfy the request $\gamma_{low} \leq \gamma' \leq \gamma$, where the lower limit is $-\pi, -\pi/2, 0$, and $\pi/2$ when γ pertains to $Q = III, IV, I$, and II , respectively [Fig. 1(d)]. Having available the $p_{H,IRR}^{(b,Q)}(K, \varphi)$ pdfs, this approach can be stated in terms of K and φ , i.e., identifying in the (K, φ) plane (limited to the $0 \leq \varphi \leq \pi/2$ range for symmetry reasons), a $D_H(\gamma)$ domain that satisfies the demand above ($\gamma_{low} \leq \gamma' \leq \gamma$)—a result achievable if a relationship connecting the rv γ' to the rv's K and φ : $\gamma' = \gamma_H(K, \varphi)$ exists. In the case of an SW particle, for which it is not possible to get such an explicit γ_H function, the connection between the rv's can be stated in

an implicit way from the request that $u_H(K, \varphi; \gamma')$ [Eq. (1a)] shows a *minimum*, i.e., from a couple of conditions,

$$u'_H = 0, \quad (7a)$$

$$u''_H > 0. \quad (7b)$$

The first one, solved with respect to K [see Eq. (1b)], provides a relationship valid for H and φ values making it positive,

$$K_H^*(\varphi; \gamma') = HJ_s \frac{\sin \gamma'}{\sin(2\varphi - 2\gamma')}. \quad (8)$$

The second one, with the constraint $K = K_H^*$, becomes [see Eq. (1c)]

$$u_H^{''*}(\varphi; \gamma') = HJ_s \sin \gamma' \left[\frac{2}{\tan(2\varphi - 2\gamma')} + \frac{1}{\tan \gamma'} \right] > 0. \quad (9)$$

By setting Eq. (9) to zero, one gets the φ values where it changes sign in the $0 \leq \varphi \leq \pi/2$ interval,

$$\varphi_0^{(Q)}(\gamma') = \gamma' - \frac{1}{2} \arctan(2 \tan \gamma') + n^{(Q)} \frac{\pi}{2}, \quad (10)$$

where $n^{(Q)} = 2, 1, 0$, and -1 when $Q = III, IV, I$, and II , respectively. Furthermore, in the $0 \leq \varphi \leq \pi/2$ range, both the K_H^* and $u_H^{''*}$ functions have a vertical asymptote at

$$\varphi_\infty^{(Q)}(\gamma') = \gamma' + n^{(Q)} \frac{\pi}{2}. \quad (11)$$

To delimit the $D_H(\gamma)$ domain (magenta regions in Fig. 5), one has to find before, for each γ' , the $\Delta_\varphi^*(\gamma')$ interval, i.e., the φ values range making $u_H(K, \varphi; \gamma')$ minimum, which is defined by the overlap region where both $K_H^*(\varphi; \gamma')$ and $u_H^{''*}(\varphi; \gamma')$ are positive. This process is described in the Appendix, for the three loop branches [Fig. 1(c)] and the four quadrants [Fig. 1(d)].

Once this is done, the $D_H(\gamma)$ domain emerges as the (φ, K) plane region swept by all the $K_H^*(\varphi; \gamma')$ functions [each of them limited to its $\Delta_\varphi^*(\gamma')$ range] for increasing γ' between γ'_{low} to γ (white curves in Fig. 5). This procedure is summarized by the \widehat{D} -operator,

$$\widehat{D}_H(\gamma) = \{K_H^*(\varphi; \gamma')\}_{\gamma'_{low}}^\gamma, \quad (12)$$

where γ'_{low} is the lower limit of the quadrant considered, as detailed in the next paragraphs.

The knowledge of $D_H(\gamma)$ allows one to write the cumulative distribution function, given H and γ , and its derivative—the probability density function,

$$P_H^{(b,Q)}(\gamma) = \iint_{D_H(\gamma)} p_{H,IRR}^{(b,Q)}(K, \varphi) dK d\varphi, \quad (13a)$$

$$p_H^{(b,Q)}(\gamma) = dP_H^{(b,Q)}(\gamma)/d\gamma, \quad (13b)$$

with the integrand reported in Fig. 3 (red curves). When performing the integration vs K in Eq. (13a), one must remember that the

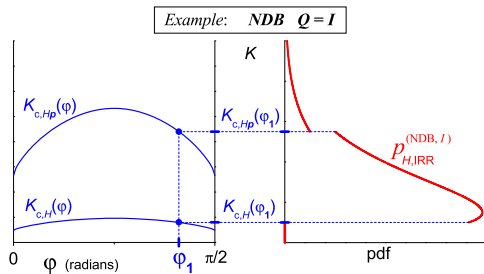


FIG. 4. An example of the “irreversible” $p_{H,IRR}^{(NDB,I)}(K, \varphi_1)$ pdf (on the right) selected by the $K_{c,H}(\varphi)$ and $K_{c,Hp}(\varphi)$ thresholds (on the left). See Fig. 3 for other cases.

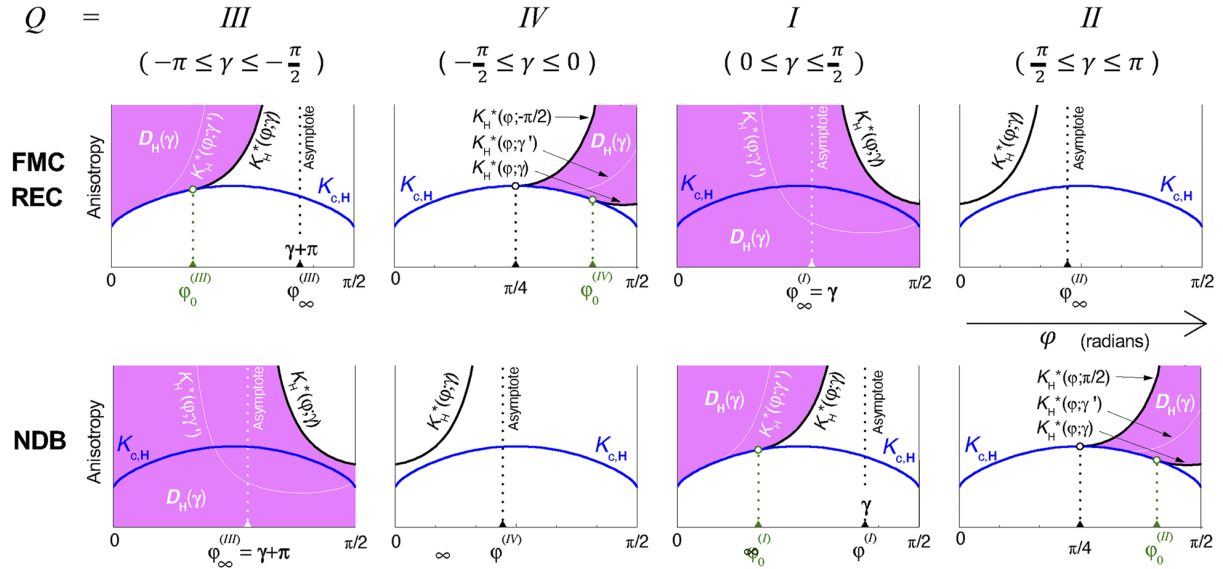


FIG. 5. The magenta regions represent the $D_H(\gamma)$ integration domains of the $P_H^{(b,Q)}$ cumulative distribution functions [Eq. (13a)], for the three “b” branches (FMC, REC, and NDB) reported in Fig. 1(c), and the four Q quadrants. Note that when $Q = II$ in FMC and REC, and $Q = IV$ in NDB, no D_H domain appears, according to the fact that, in these conditions, the local \tilde{J}_s cannot find any stable equilibrium orientation. In $Q = IV$ of FMC and REC, and in $Q = II$ of NDB, the top-left D_H border is correspondingly given by the function $K_H^*(\varphi; \mp\pi/2) = |H|J_s/\sin(2\varphi)$ [Eq. (8) with $\gamma' = \mp\pi/2$], with asymptotes $\varphi = \pi/2$ in both cases. Observe the thin white curves $K_H^*(\varphi; \gamma')$, whose evolution from γ'_{low} to γ (thick black curves) devises the $D_H(\gamma)$ regions.

thresholds $K_{c,H}(\varphi)$ and $K_{c,Hp}(\varphi)$ [see Eq. (4)] indicate, for each φ , the K values where the $p_{H,IRR}^{(b,Q)}(K, \varphi)$ pdf changes, as discussed in Sec. III A 4. As an example, Fig. 4 displays the case $Q = I$ across NDB.

1. First magnetization curve (FMC)

According to Sec. III A 4 and Fig. 3(b), along this branch, the $K_{c,Hp}(\varphi)$ curves do not play any role (and thus are not depicted in Fig. 5), whereas the $K_{c,H}(\varphi)$ ones not only signal the K thresholds where the $p_{H,IRR}^{(FMC,Q)}$ pdfs [retrieved from Fig. 3(b)] change but also represent a portion of the D_H integration domains (magenta regions in Fig. 5, for $Q = III$ and $Q = IV$) border.

a) $-\pi \leq \gamma \leq -\pi/2$ ($Q = III$)

The $D_H(\gamma)$ domain is obtained employing the \hat{D} -operator [Eq. (12)] with $\gamma'_{low} = -\pi$. Being $\varphi_\infty^{(III)}(\gamma) = \gamma + \pi$ [Eq. (11) with $n^{(Q)} = 2$], Eq. (13a) becomes

$$P_H^{(FMC,III)}(\gamma) = \int_0^{\varphi_0^{(III)}(\gamma)} \int_{K_{c,H}(\varphi)}^\infty p_{H,IRR}^{(FMC,III)}(K, \varphi) dK d\varphi + \int_{\varphi_0^{(III)}(\gamma)}^{\gamma+\pi} \int_{K_H^*(\varphi; \gamma)}^\infty p_{H,IRR}^{(FMC,III)}(K, \varphi) dK d\varphi. \quad (14)$$

Observing [Eq. (8)] that $K_H^*(\gamma + \pi; \gamma) \rightarrow \infty$ (where any pdf vanishes), and considering Eq. (A2), Eq. (13b) becomes

$$p_H^{(FMC,III)}(\gamma) = \int_{\gamma+\pi}^{\varphi_0^{(III)}(\gamma)} \mathfrak{Z}_H^{(FMC,III)}(\varphi; \gamma) d\varphi, \quad (15)$$

where $\varphi_0^{(III)}$ is supplied by Eq. (10) with $\gamma' = \gamma$ and $n^{(Q)} = 2$, and the integrand is defined as follows:

$$\mathfrak{Z}_H^{(FMC,III)}(\varphi; \gamma) := p_{H,IRR}^{(FMC,III)}[K_H^*(\varphi; \gamma), \varphi] \frac{\partial K_H^*(\varphi; \gamma)}{\partial \gamma}, \quad (16)$$

with

$$\frac{\partial K_H^*(\varphi; \gamma)}{\partial \gamma} = HJ_s \frac{\cos \gamma \sin(2\varphi - 2\gamma) + 2 \sin \gamma \cos(2\varphi - 2\gamma)}{\sin^2(2\varphi - 2\gamma)} \quad (17)$$

b) $-\pi/2 \leq \gamma \leq 0$ ($Q = IV$)

The $D_H(\gamma)$ domain is obtained by utilizing the \hat{D} -operator [Eq. (12)] with $\gamma'_{low} = -\pi/2$. The top-left border of $D_H(\gamma)$ is given [Eq. (8)] by the curve $K_H^*(\varphi; -\pi/2) = HJ_s/\sin 2\varphi$, with asymptote $\varphi = \pi/2$ —a value not accounted for by Eq. (11). The cumulative and density functions [the second one remembering again Eq. (A2)] become

$$P_H^{(FMC,IV)}(\gamma) = \int_{\pi/4}^{\varphi_0^{(IV)}(\gamma)} \int_{K_{c,H}(\varphi)}^{K_H^*(\varphi; -\pi/2)} p_{H,IRR}^{(FMC,IV)}(K, \varphi) dK d\varphi + \int_{\varphi_0^{(IV)}(\gamma)}^{\pi/2} \int_{K_H^*(\varphi; \gamma)}^{K_H^*(\varphi; -\pi/2)} p_{H,IRR}^{(FMC,IV)}(K, \varphi) dK d\varphi, \quad (18)$$

$$p_H^{(FMC,IV)}(\gamma) = \int_{\pi/2}^{\varphi_0^{(IV)}(\gamma)} \mathfrak{Z}_H^{(FMC,IV)}(\varphi; \gamma) d\varphi, \quad (19)$$

with $\varphi_0^{(III)}$ given by Eq. (10) with $\gamma' = \gamma$ and $n^{(Q)} = 1$, and the integrand defined similarly as in $Q = III$ [Eqs. (16) and (17)]

c) $0 \leq \gamma \leq \pi/2$ ($Q = I$)

The $D_H(\gamma)$ domain is obtained using the \widehat{D} -operator [Eq. (12)] with γ' increasing from $\gamma'_{low} = 0$. The cumulative function [being $\varphi_\infty(\gamma) = \gamma$ from Eq. (11) with $n^{(Q)} = 0$], and the pdf associated [observing that $K_H^*(\gamma; \gamma) \rightarrow \infty$, from Eq. (8)] become

$$P_H^{(FMC,I)}(\gamma) = \int_0^\gamma \int_0^\infty P_{H,IRR}^{(FMC,I)}(K, \varphi) dK d\varphi + \int_\gamma^{\pi/2} \int_0^{K_H^*(\varphi; \gamma)} P_{H,IRR}^{(FMC,I)}(K, \varphi) dK d\varphi, \quad (20)$$

$$p_H^{(FMC,I)}(\gamma) = \int_\gamma^{\pi/2} \mathfrak{Z}_H^{(FMC,I)}(\varphi; \gamma) d\varphi, \quad (21)$$

again with the integrand defined similarly as in $Q = III$ [Eqs. (16) and (17)].

d) $\pi/2 \leq \gamma \leq \pi$ ($Q = II$)

As discussed in the Appendix, the absence of a stable equilibrium orientation for the local \vec{f}_s is reflected in the lack of the integration domain D_H , and agrees with the fact that, in this region, we have $p_H^{(FMC,II)} = 0$ (Sec. III A and Fig. 2). Therefore,

$$p_H^{(FMC,II)}(\gamma) = 0. \quad (22)$$

2. Recoil curve (REC)

The very same path driving to the FMC pdfs can be adopted here, the $K_{c,H}$ threshold decreasing with H , from K_{c,H_p} to zero. However, as shown in Fig. 3(c), due to the absence of IRs along this branch, the “irreversible” pdfs are frozen to the last value reached across FMC, i.e., when $H = H_p$,

$$p_{H,IRR}^{(REC,Q)} = p_{H_p,IRR}^{(FMC,Q)} \quad (23)$$

for all Q quadrants. Accordingly, the integrands [Eq. (16)] turn into

$$\mathfrak{Z}_H^{(REC,Q)}(\varphi; \gamma) = p_{H_p,IRR}^{(FMC,Q)} [K_H^*(\varphi; \gamma), \varphi] \frac{\partial K_H^*(\varphi; \gamma)}{\partial \gamma}, \quad (24)$$

with the derivative given by Eq. (17).

3. Negative descending branch (NDB)

Along this branch, a very similar and, to some extent, specular scenario (specular to the FMC and REC cases) appears, with the D_H shapes in $Q = III, IV, I$, and II recovering the ones found along FMC (or REC) in $Q = I, II, III$, and IV , respectively, but with different φ integration limits (see Fig. 5). Now, the top-left border of D_H in $Q = II$ is given [Eq. (8)] by the curve $K_H^*(\varphi; \pi/2) = -HJ_s/\sin 2\varphi$, with asymptote $\varphi = \pi/2$ —a value not accounted for by Eq. (11). Thus, a procedure like the one described above supplies the γ pdfs for the four quadrants,

$$p_H^{(NDB,III)}(\gamma) = \int_{\gamma+\pi}^{\pi/2} \mathfrak{Z}_H^{(NDB,III)}(\varphi; \gamma) d\varphi, \quad (25a)$$

“b” branch	Q	III	IV	I	II
	$n^{(Q)}$	2	1	0	-1
FMC	$\varphi_0^{(b,Q)}$	$\varphi_0^{(III)}$	$\varphi_0^{(IV)}$	$\pi/2$	0
REC	$\varphi_{LOW}^{(b,Q)}$	$\gamma + \pi$	$\pi/2$	γ	0
NDB	$\varphi_{HIGH}^{(b,Q)}$	$\pi/2$	0	$\varphi_0^{(I)}$	$\varphi_0^{(II)}$
	$\varphi_{LOW}^{(b,Q)}$	$\gamma + \pi$	0	γ	$\pi/2$

FIG. 6. Limits of the integral appearing in Eq. (26), for the FMC, REC, and NDB branches of the hysteresis loop [see Fig. 1(c)], and the Q quadrants. The threshold $\varphi_0^{(Q)}(\gamma)$ is given by Eq. (10), with $\gamma' = \gamma$.

$$p_H^{(NDB,IV)}(\gamma) = 0, \quad (25b)$$

$$p_H^{(NDB,I)}(\gamma) = \int_\gamma^{\varphi_0^{(I)}(\gamma)} \mathfrak{Z}_H^{(NDB,I)}(\varphi; \gamma) d\varphi, \quad (25c)$$

$$p_H^{(NDB,II)}(\gamma) = \int_{\pi/2}^{\varphi_0^{(II)}(\gamma)} \mathfrak{Z}_H^{(NDB,II)}(\varphi; \gamma) d\varphi, \quad (25d)$$

with the $\mathfrak{Z}_H^{(NDB,Q)}$ defined similarly to $\mathfrak{Z}_H^{(FMC,Q)}$, and the $p_{H,IRR}^{(NDB,Q)}(K, \varphi)$ values changing over both the thresholds $K_{c,H}(\varphi)$ and $K_{c,H_p}(\varphi)$, as shown in Fig. 3(d).

4. Compact expression for the $p_H^{(b,Q)}(\gamma)$ pdfs

It is possible to write the pdfs for the local \vec{f}_s making an angle γ with \vec{H} in a very compact integral form, depending on the “b” branch (FMC, REC, or NDB) and the Q (=III, IV, I, and II) quadrant occupied by the equilibrium angle γ ,

$$p_H^{(b,Q)}(\gamma) = \int_{\varphi_{LOW}^{(b,Q)}}^{\varphi_{HIGH}^{(b,Q)}} \mathfrak{Z}_H^{(b,Q)}(\varphi; \gamma) d\varphi, \quad (26)$$

with

$$\mathfrak{Z}_H^{(b,Q)}(\varphi; \gamma) := p_{H,IRR}^{(b,Q)} [K_H^*(\varphi; \gamma), \varphi] \frac{\partial K_H^*(\varphi; \gamma)}{\partial \gamma}. \quad (27)$$

The $p_{H,IRR}^{(b,Q)}$ are retrieved from Fig. 3 [remember Eq. (23) as well], the derivative from Eq. (17), and the integration limits summarized in the scheme of Fig. 6. In it, to make Eq. (26) formally valid for any “b” and “Q,” the integration limits of $Q = II$ in FMC and REC and of $Q = IV$ in NDB are “artificially” put equal to zero, thus obtaining $p_H^{(FMC,II)} = p_H^{(REC,II)} = p_H^{(NDB,IV)} = 0$.

5. Constitutive law and hysteresis loop

Considering a particle assembly magnetized by an alternating quasi-static field, from the constitutive equation, calculated over the whole γ domain,

$$J^{(b)}(H) = J_s \int_{-\pi}^{\pi} p_H^{(b,Q)}(\gamma) \cos \gamma d\gamma, \quad (28)$$

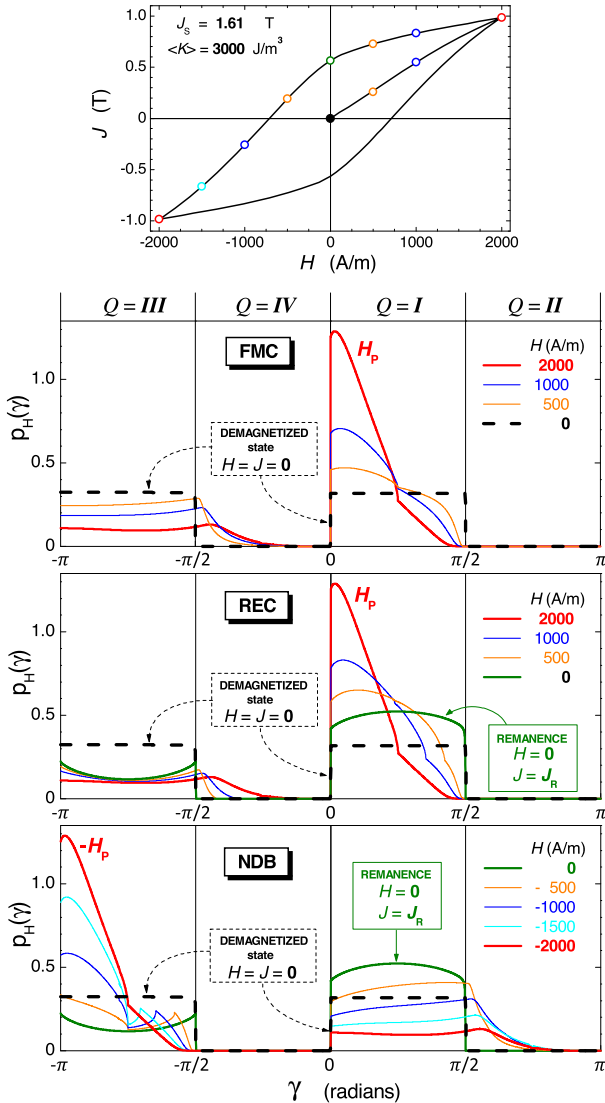


FIG. 7. When a quasi-static alternating field is applied, the evolution of $p_H(\gamma)$ [Eqs. (26) and (27)] is displayed for the FMC, REC, and NDB branches [Eq. (28)] of the hysteresis loop drawn on the top, where the fields in correspondence of which the $p_H(\gamma)$ are calculated are marked with open dots of the same color. The dashed black lines represent the demagnetized state ($H = J = 0$) realized when Eq. (6) is satisfied. On the other extreme, $p_H(\gamma)$ becomes the Dirac delta function $\delta_D(\gamma)$ or $\delta_D(\gamma + \pi)$ when $H \rightarrow \pm\infty$, respectively. Observe the symmetry of the $p_H(\gamma)$ corresponding to the $\pm H_p$ peak fields.

with $p_H^{(b,Q)}$ given by Eq. (26), the hysteresis loop is drawn, and the corresponding energy loss W is given by its area. Moreover, as described below (Sec. IV), it is also possible to work out a semi-empirical but very accurate integral expression for W not entailing the knowledge of the hysteresis loop.

Figure 7 shows, for the whole $-\pi \leq \gamma \leq \pi$ range, an example of $p_H^{(b,Q)}(\gamma)$ vs H evolution, calculated with Eq. (26), and the corresponding hysteresis loop [Eq. (28)] with $J_s = 1.61$ T. We have

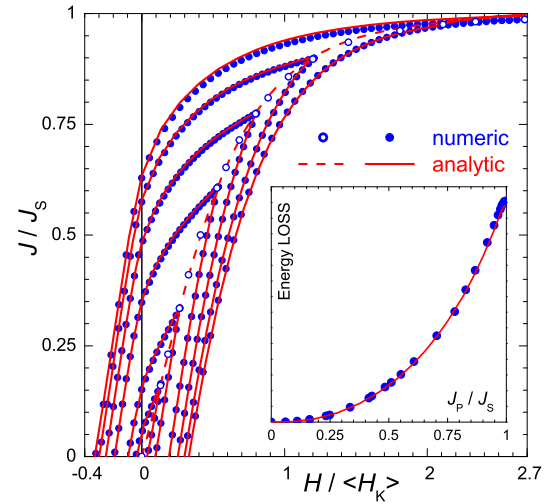


FIG. 8. Alternating quasi-static magnetizing field. The excellent agreement between the First Magnetization Curve (open dots and dashed lines) and the hysteresis loops numerically found, and the ones obtained via the statistical method, are displayed ($\langle H_K \rangle = 2\langle K \rangle / J_s$; $J_s = |\bar{J}_s|$). The inset shows the behavior of losses, with the red curve representing both the values given by the loop areas and the empirical ones of Eq. (33), this last plotted in correspondence with the $J_p(H_p)$ peak polarizations of Eq. (34). One cannot appreciate significant differences between the two loss figures.

assumed $\psi(K, \varphi) = f(K)g(\varphi)$, with the marginal pdfs supplied by Eqs. (5a) and (5b) and $\langle K \rangle = 3000$ J/m³.

The effectiveness of the statistical method is apparent in Fig. 8, where the quasi-static hysteresis loops, computed at different peak polarization J_p using Eq. (28) and the corresponding loss figures (inset), perfectly recover the ones obtained via the numerical procedure presented in Sec. II B [again it is assumed $\psi(K, \varphi) = f(K)g(\varphi)$, with the marginal pdfs furnished by Eqs. (5a) and (5b)].

6. Elemental hysteresis loops

The statistical approach developed was dictated by the impossibility to solve Eq. (8) with respect to the γ equilibrium angle for the local polarization \bar{J}_s [see Fig. 1(a)]—a goal that would directly supply the analytic expression for the elemental loops associated with a single particle. This difficulty has been circumvented by the mathematical technique outlined above, which supplies, in a sense, a “statistical solution” of Eq. (8), working out $p_H(\gamma)$, the probability to find \bar{J}_s laid along the γ direction. In this framework, the elemental hysteresis loops corresponding to a particle characterized by $\varphi = \varphi_1$ and $K = K_1$ come out defining the K and φ joint statistics as follows:

$$\psi(K, \varphi) = \delta_D(K - K_1) \delta_D(\varphi - \varphi_1), \quad (29)$$

where δ_D is the Dirac delta function.

As usual, the starting point is the demagnetized state (DEM), identified by Eq. (6), which can now be rewritten in terms of γ , for any K_1 ,

$$p_{DEM}^{(Q=I)}(\gamma) = \frac{1}{2} \delta_D[\gamma - \varphi_1], \quad (30a)$$

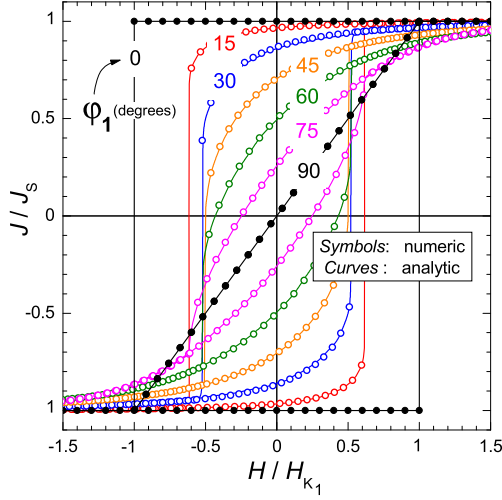


FIG. 9. Alternating quasi-static magnetizing field. For different φ_1 angles between the local easy axis \vec{K} and the \vec{H} applied field direction ($H_{K1} = 2K_1/J_s$; $J_s = |\vec{J}_s|$), it is apparent the capacity of the statistical approach to perfectly cover the elemental hysteresis loops obtained through the numerical procedure outlined in Sec. II B.

$$p_{DEM}^{(Q=III)}(\gamma) = \frac{1}{2} \delta_D[\gamma - (\varphi_1 - \pi)], \quad (30b)$$

$$p_{DEM}^{(Q=II)}(\gamma) = p_{DEM}^{(Q=IV)}(\gamma) = 0. \quad (30c)$$

For increasing $H \leq H_{c,K1}(\varphi_1)$ [Eq. (3)], all the local \vec{J}_s reversibly rotate toward $\gamma = 0$ [in particular, the \vec{J}_s belonging to the third quadrant when $H = 0$ remains confined in it if $\varphi \leq \pi/4$ or, when $\varphi > \pi/4$,

as long as $H \leq H_{III \rightarrow IV}$ (see Sec. III A 1)], and no loop appears. When the alternating H overcomes the inversion field $H_p = H_{c,K1}(\varphi_1)$, the \vec{J}_s particles in $Q = III$ or $Q = IV$ jump to the first quadrant in the $0 \leq \gamma \leq \varphi_1$ range [with $p_H(\gamma) \rightarrow \delta_D(\gamma)$ when $H \rightarrow +\infty$]. A similar and, to some extent, specular behavior is found following the recoil curve and the negative descending branch.

The ability of the analytic procedure to reproduce the elemental loops obtained when H oscillates with peak values $|H_p| = H_{c,K}(\varphi_1)$ [Eq. (3)] and $J = J_s \cos \gamma$ measured along the \vec{H} direction is apparent in Fig. 9, from the comparison with the cycles numerically computed.

IV. ENERGY LOSS: AN APPROXIMATE INTEGRAL EXPRESSION

Let us consider the elemental hysteresis loops introduced above (Sec. III B 6), with local coercive fields $\pm H_{c,K}(\varphi)$ [Eq. (3)], peak polarization $J_p(\varphi)$, remanence $J_r(\varphi)$, and loss W . Now, we take as peak value the polarization reached immediately after the irreversible switch occurring at $H_{c,K}$ under increasing field: $J_p(\varphi) := J[H_{c,K}^+]$ (a larger H moves J along a reversible branch, non-modifying the loop area). An example obtained for $\varphi = 35^\circ$ ($J_s = 1$ T, $K = 1$ J/m³) is given by the green solid line in Fig. 10(a), where instead the orange dashed rectangle corresponds to the case where irreversible rotations (180° switches between φ and $\varphi - \pi$ of the local \vec{J}_s) only are present. The area (giving the energy loss in J/m³) of the latter, with peak irreversible polarization $J_{IRR,p} \equiv J_r = J_s \cos \varphi$, is supplied by the following relationship:

$$W_{IRR}(K, \varphi) = 2H_{c,K}(\varphi) \cdot 2J_r(\varphi) = 8K \frac{\cos \varphi}{A(\varphi)}, \quad (31)$$

which is obtained from Eq. (3), and with $A(\varphi)$ given by Eq. (2).

For any φ , the difference between W and W_{IRR} is concentrated in the gray pseudo-triangles with vertices $\pm J_r$, $\pm J_c$, and $\pm J_p$ [Fig. 10(a)]: all linear quantities dependent on J_s and independent

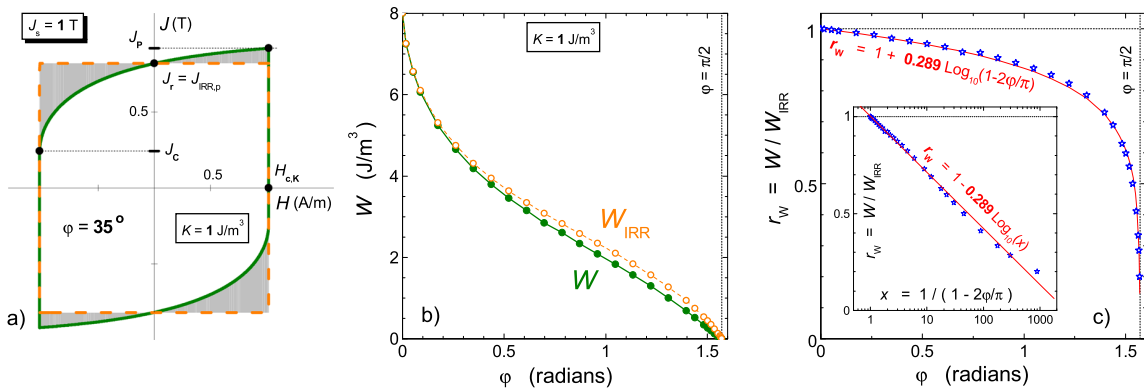


FIG. 10. (a) The continuous green line describing the elemental hysteresis loop transforms into the dashed orange rectangle when only irreversible rotations are accounted for ($J_s = 1$ T, $K = 1$ J/m³, $\varphi = 35^\circ$, $H_{c,K}(\varphi) = 1.02$ A/m, $J_c = 0.243$ T, $J_r = 0.819$ T, $J_p = 0.92$ T). The difference between the loop areas is put in evidence by the gray pseudo-triangles. (b) Behavior vs φ of the loss W , and its irreversible component W_{IRR} (both independent of J_s), of the corresponding elemental loops. For $\varphi = 0$, the absence of irreversible processes entails $W = W_{IRR} = 8K$ [Eq. (31)]. (c) Interpolation of the K independent quantity W/W_{IRR} vs φ , obtained (see inset) through the least squares linear fit of such a ratio vs $\log_{10}[1/(1 - \frac{2}{\pi}\varphi)]$.

of K [$J_r = J_s \cos \varphi$, and for J_c and J_p , see Eqs. (8.34), (8.38), and (8.41) of Ref. 5]. Being $H_{c,K}$ [Eq. (3)] inversely proportional to J_s , as this last varies the loops aspect ratio modifies, but W and W_{IRR} [Eq. (31)] do not. Moreover, $H_{c,K}$ is the same for both loops, and one gets $W_{IRR}(aK, \varphi) = aW_{IRR}(K, \varphi)$ and $W(aK, \varphi) = aW(K, \varphi)$. For the arguments above, the ratio between the two losses [these last plotted in Fig. 10(b)] turns out to be φ dependent only, as reported in Fig. 10(c), where it is interpolated by the following *general empirical law*:

$$r_W(\varphi) := \frac{W(K, \varphi)}{W_{IRR}(K, \varphi)} = 1 + 0.289 \log_{10} \left(1 - \frac{2}{\pi} \varphi \right), \quad (32)$$

with the coefficient 0.289 found via a least square linear fit of W/W_{IRR} vs $\log_{10}[1/(1 - \frac{2}{\pi} \varphi)]$ [Fig. 10(c) inset].

Eventually, for $H = H_p$, the energy loss of the whole particle ensemble is obtained after integration over the anisotropy axes values and orientations [from Eqs. (31) and (32), and with K_{c,H_p} given by Eq. (4)],

$$\begin{aligned} W(H_p) &= \int_0^{\pi/2} \int_0^{K_{c,H_p}(\varphi)} \psi(K, \varphi) W(K, \varphi) dK d\varphi \\ &= 8 \int_0^{\pi/2} r_W(\varphi) \frac{\cos \varphi}{A(\varphi)} \int_0^{K_{c,H_p}(\varphi)} \psi(K, \varphi) K dK d\varphi. \end{aligned} \quad (33)$$

One can also formulate this expression in terms of the peak induction corresponding to H_p , calculated on the First Magnetization Curve with Eq. (28),

$$J_p := J^{(FMC)}(H_p) = J_s \int_{-\pi}^{\pi} P_{H_p}^{(FMC,Q)}(\gamma) \cos \gamma d\gamma. \quad (34)$$

The energy loss values supplied by Eq. (33) are almost identical to the ones given by the hysteresis loops areas, as shown in the inset of Fig. 8.

V. CONCLUSIONS

The developed mathematical tool analytically predicts the response of an assembly of non-interacting SW particles driven by a quasi-static alternating magnetic field. The exact integral relationships for the hysteresis loops and losses allow one to bypass the computationally slow numeric procedure necessary to implement the SW model in software used to predict the behavior of devices containing magnetic components.

The versatility of this approach lies in its skills listed below.

- (1) It works with any anisotropy distribution, permitting one to easily predict the role played by the sample texture (e.g., the effect of a macroscopic easy axis induced either by annealing or by applied stress).
- (2) The same analytic-statistical procedure, although more complicated, can be exploited with any field history (e.g., rotating fields,^{31,34} loops with bias, and asymmetrical minor loops).
- (3) Marginal modifications of the approach allow it to account for the presence of domain walls inside the particles, following the idea suggested in Ref. 22.
- (4) The whole mathematical structure is prone to a generalization for systems of particles endowed with biaxial anisotropy.

- (5) Under whatever field history and accounting for interactions, in Ref. 40, a mathematical technique capable to track the irreversible switches in a particle assembly described by the SW model has been worked out (so preserving the non-local memory of the system), together with a graphic representation that turns out to be an extension of the one operating in the Preisach model. One can then envisage a coupling between such a tool and the one developed here, with the aim to assess a more general analytical approach to the particle systems description.

ACKNOWLEDGMENTS

This research work was carried out in the framework of the Grant No. 19ENG06 HEFMAG project, which was funded by the EMPIR program, and co-financed by the Participating States and the European Union's Horizon 2020 research and innovation program.

AUTHOR DECLARATIONS

Conflict of Interest

The author has no conflicts to disclose.

Author Contributions

C. Appino: Conceptualization (lead); Data curation (lead); Formal analysis (lead); Investigation (lead); Methodology (lead); Software (lead); Supervision (lead); Validation (lead); Visualization (lead); Writing – original draft (lead); Writing – review & editing (lead).

DATA AVAILABILITY

The data that support the findings of this study are available within the article.

APPENDIX: MINIMA OF THE GIBBS FREE ENERGY DENSITY u_H VS THE ANISOTROPY AXIS ORIENTATION φ

For a general γ' equilibrium orientation of \vec{J}_s , with $\gamma'_{low} \leq \gamma' \leq \gamma$ (where γ depends on the Q quadrant considered, and γ'_{low} is its lower limit), the $\Delta_\varphi^*(\gamma')$ range, corresponding to a minimum of the particle Gibbs energy $u_H(K, \varphi; \gamma')$ [Eq. (1a)], is determined by the overlap between two φ regions: the first one, where $K_H^*(\varphi; \gamma')$ [Eq. (8)] is positive, and the second one satisfying Eq. (9), $u_H^{**}(\varphi; \gamma') > 0$, as illustrated in Fig. 11 (remember that φ is limited between 0 and $\pi/2$ for symmetry reasons).

The $\Delta_\varphi^*(\gamma')$ interval is found before for the field values $0 \leq H \leq H_p$, i.e., when the First Magnetization Curve (FMC) and the RECoil curve (REC) are covered (upper strip of Fig. 11). In this case, for $Q = III$ and $Q = IV$, the two regions partially overlap, and the $\Delta_\varphi^*(\gamma')$ limits are $[\varphi_0^{(III)}; \varphi_\infty^{(III)} = \gamma' + \pi]$ and $[\varphi_0^{(IV)}; \pi/2]$, respectively [see Eqs. (10) and (11)]. In $Q = I$, the entire region where $K_H^* > 0$ falls in the range where $u_H^{**} > 0$; $\varphi_0^{(I)}$, which drops outside, does not play any role, and the $\Delta_\varphi^*(\gamma')$ limits are $[\varphi_\infty^{(I)}; \pi/2]$. Eventually, in $Q = II$, the two regions do not overlap, signaling the fact that, in this

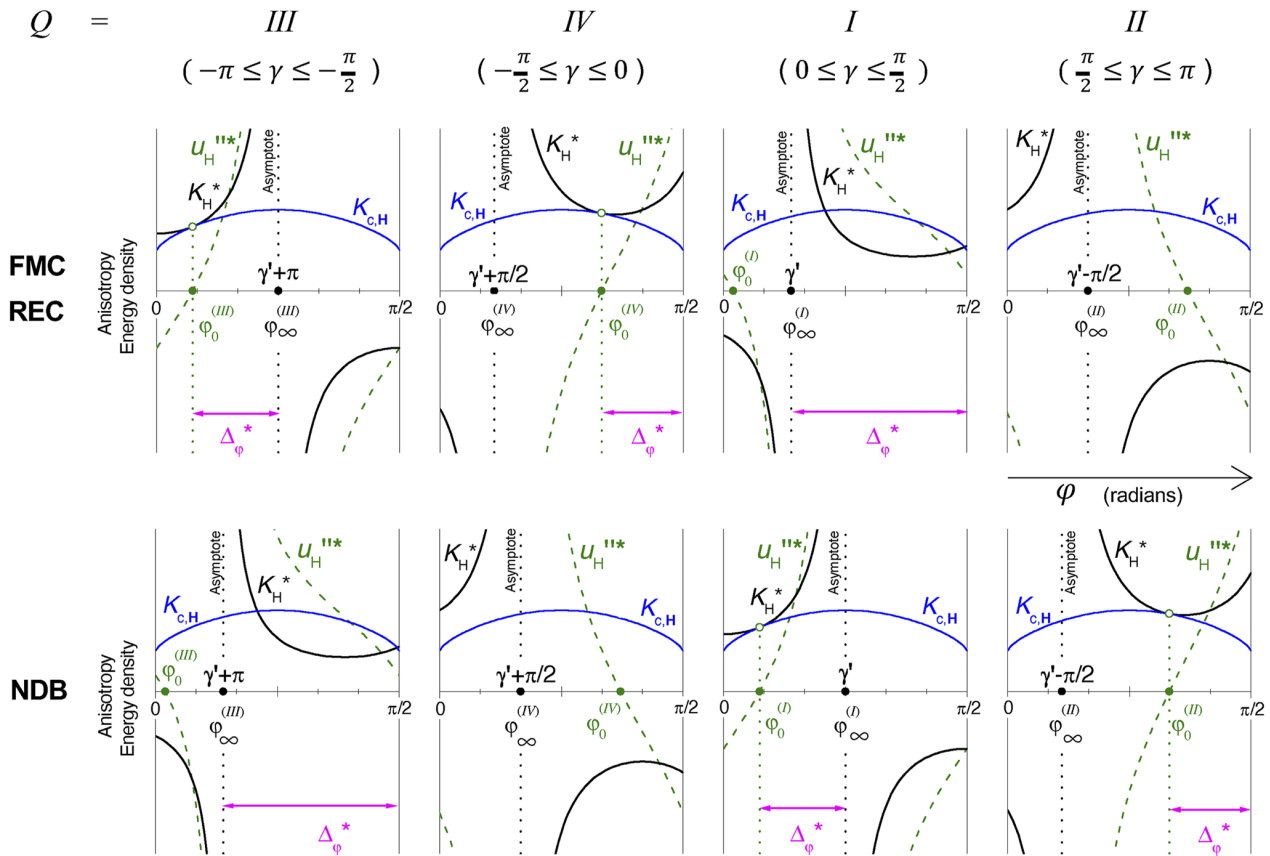


FIG. 11. The $\Delta_\phi^*(\gamma')$ intervals, where the Gibbs free energy $u_H(K, \phi; \gamma')$ of a “particle” displays a minimum, are shown for each branch and quadrant (note that no Δ_ϕ^* exists for $Q = II$ in FMC or REC, and for $Q = IV$ in NDB). The values of $\phi_0^{(Q)}(\gamma')$ and of the asymptotes $\phi_\infty^{(Q)}(\gamma')$ of $K_H^*(\phi; \gamma')$ and $u_H^{**}(\phi; \gamma')$ are given by Eqs. (10) and (11), respectively. In the case $Q = I$ for FMC and REC, the picture displays the situation occurring when $\gamma \leq \pi/4$, corresponding to the of K_H^* and $u_H^{**,*}$ crossing. A similar situation is found in the case $Q = III$ for NDB, when $\gamma \leq -3\pi/4$.

quadrant, no stable equilibrium position for \vec{f}_s exists. This fact agrees with the result $p_{H,IRR}^{(FMC,II)} = 0$, which is reported at the end of Sec. III A, and is derived simply by observing the system geometry [Fig. 1(a)].

When $H < 0$ (lower strip of Fig. 11), i.e., along the Negative Descending Branch (NDB), a very similar and, to some extent, specular scenario appears—the situations in $Q = III, IV, I$, and II now recovering the ones found along FMC and REC in $Q = I, II, III$, and IV , respectively.

Eventually, let us contemplate the case when $\phi_0^{(Q)}$ constitutes the lower limit of the $\Delta_\phi^*(\gamma')$ interval ($Q = III$ and $Q = IV$ for FMC and REC, and $Q = I$ and $Q = II$ for NDB). In this circumstance, inserting the $\phi_0^{(Q)}$ value [Eq. (10)] into Eq. (8), one gets (considering that $K > 0$)

$$K_H^*[\phi_0^{(Q)}(\gamma'); \gamma'] = J_s \left| H \frac{\sin \gamma'}{\sin [\arctan(2 \tan \gamma')]} \right|, \quad (A1)$$

a quantity that, together with function (10), constitutes a couple of parametric equations (with γ' parameter) identifying, in the (ϕ, K)

plane, a curve that coincides with $K_{c,H}$, being this last obtained under the conditions $u_H' = u_H'' = 0$, as well. Consequently, $\phi_0^{(Q)}$ represents the abscissa of the tangent point between K_H^* and $K_{c,H}$, and one gets

$$K_H^*[\phi_0^{(Q)}(\gamma'); \gamma'] = K_{c,H}[\phi_0^{(Q)}(\gamma')], \quad (A2)$$

an essential result for the calculation leading to $p_H(\gamma)$, in Sec. III B 1.

REFERENCES

- ¹R. C. O’Handley, *Modern Magnetic Materials: Principles and Applications* (Wiley-Interscience, New York, 1999).
- ²F. Fiorillo, G. Bertotti, C. Appino, and M. Pasquale, “Soft magnetic materials,” in *Wiley Encyclopedia of Electrical and Electronics Engineering*, edited by M. Peterca (John Wiley and Sons, Hoboken, NJ, 2016).
- ³F. Fiorillo, C. Appino, and M. Pasquale, “Hysteresis in magnetic materials,” in *The Science of Hysteresis*, edited by G. Bertotti and I. Mayergoyz (Academic Press, Amsterdam, 2006), Vol. III.

- ⁴E. C. Stoner and E. P. Wohlfarth, "A mechanism of magnetic hysteresis in heterogeneous alloys," *Philos. Trans. R. Soc. London, Ser. A* **240**, 599 (1948).
- ⁵G. Bertotti, *Hysteresis in Magnetism* (Academic Press, New York, 1998).
- ⁶C. Tannous and J. Gieraltowski, "The Stoner–Wohlfarth model of ferromagnetism," *Eur. J. Phys.* **29**, 475 (2008).
- ⁷J. C. Slonczewski, "Theory of magnetic hysteresis in films and its application to computers," *IEEE Trans. Magn.* **45**(1), 8 (2009).
- ⁸F. Liorzou, B. Phelps, and D. L. Atherton, "Macroscopic models of magnetization," *IEEE Trans. Magn.* **36**(2), 418 (2000).
- ⁹A. Tamion, E. Bonet, F. Tournus, C. Raufast, A. Hillion, O. Gaier, and V. Dupuis, "Efficient hysteresis loop simulations of nanoparticle assemblies beyond the uniaxial anisotropy," *Phys. Rev. B* **85**, 134430 (2012).
- ¹⁰V. M. Kalita, A. I. Tovstolytkin, S. M. Ryabchenko, O. V. Yelenich, S. O. Solopan, and A. G. Belous, "Mechanisms of AC losses in magnetic fluids based on substituted manganites," *Phys. Chem. Chem. Phys.* **17**, 18087 (2015).
- ¹¹S. V. Komogortsev, D. A. Balaev, A. A. Krasikov, S. V. Stolyar, R. N. Yaroslavl'tsev, V. P. Ladygina, and R. S. Iskhakov, "Magnetic hysteresis of blocked ferrihydrite nanoparticles," *AIP Adv.* **11**, 015329 (2021).
- ¹²R. Delgado-García, G. Rodríguez-Rodríguez, and J. M. Colino, "Improved averaging of hysteresis loops from micromagnetic simulations of non-interacting uniaxial nanoparticles," *AIP Adv.* **11**, 015137 (2021).
- ¹³M. Coisson, G. Barrera, C. Appino, F. Celegato, L. Martino, A. P. Safronov, G. V. Kuryandskaya, and P. Tiberto, "Specific loss power measurements by calorimetric and thermal methods on γ -Fe₂O₃ nanoparticles for magnetic hyperthermia," *J. Magn. Magn. Mater.* **473**, 403 (2019).
- ¹⁴M. Anand, "Hysteresis in a linear chain of magnetic nanoparticles," *J. Appl. Phys.* **128**, 023903 (2020).
- ¹⁵T. M. L. Alves, C. G. Bezerra, A. D. C. Viegas, S. Nicolodi, M. A. Corrêa, and F. Bohn, "Quantifying magnetic anisotropy dispersion: Theoretical and experimental study of the magnetic properties of anisotropic FeCuNbSiB ferromagnetic films," *J. Appl. Phys.* **117**, 083901 (2015).
- ¹⁶A. Kuncser, G. Schintze, C. Ghica, S. Antohe, and V. Kuncser, "Applicability of the Stoner–Wohlfarth model for Ni–Fe graded thin films," *J. Supercond. Novel Magn.* **28**, 965 (2015).
- ¹⁷J. L. F. Cuñado, A. Bollero, T. Pérez-Castañeda, P. Perna, F. Ajejas, J. Pedrosa, A. Gudín, A. Maldonado, M. A. Niño, R. Guerrero, D. Cabrera, F. J. Terán, R. Miranda, and J. Camarero, "Emergence of the Stoner–Wohlfarth astroid in thin films at dynamic regime," *Sci. Rep.* **7**, 13474 (2017).
- ¹⁸D. M. Forrester, E. Kovacs, K. E. Kürten, and F. V. Kusmartsev, "Astroid curves for a synthetic antiferromagnetic stack in an applied magnetic field," *Int. J. Mod. Phys. B* **23**(20–21), 4021 (2009).
- ¹⁹J. M. Lee and S. H. Lim, "Phase diagram of magnetization switching in a nanostructured magnetic thin film," *J. Appl. Phys.* **108**, 073910 (2010).
- ²⁰S. Ikegawa, F. B. Mancoff, J. Janesky, and S. Aggarwal, "Magnetoresistive random access memory: Present and future," *IEEE Trans. Electron Devices* **67**(4), 1407 (2020).
- ²¹E. Callen, Y. J. Liu, and J. R. Cullen, "Initial magnetization, remanence, and coercivity of the random anisotropy amorphous ferromagnet," *Phys. Rev. B* **16**(1), 263 (1977).
- ²²C. Appino, M. Valsania, and V. Basso, "A vector hysteresis model including domain wall motion and coherent rotation," *Physica B* **275**, 103 (2000).
- ²³E. Girt, K. M. Krishnan, G. Thomas, E. Girt, and Z. Altounian, "Coercivity limits and mechanism in nanocomposite Nd–Fe–B alloys," *J. Magn. Magn. Mater.* **231**, 219 (2001).
- ²⁴J. Yin, S. Zhang, H. Zhang, and B. Shen, "Application of a mean field Stoner–Wohlfarth model in nanocrystalline ribbons," *J. Phys. D: Appl. Phys.* **34**, 525 (2001).
- ²⁵A. Kuncser and V. Kuncser, "Magnetization reversal via a Stoner–Wohlfarth model with bi-dimensional angular distribution of easy axis," *J. Magn. Magn. Mater.* **395**, 34 (2015).
- ²⁶J. Zhong, Y. Guo, J. Zhu, and Z. W. Lin, "Magnetization modeling of SMC material with rotating fluxes," *Jpn. Soc. Appl. Electromagn. Mech.* **15**, S104 (2007).
- ²⁷W. Xu, N. Duan, S. Wang, Y. Guo, and J. Zhu, "A stress-dependent magnetic hysteresis model for soft magnetic composite materials," *IEEE Trans. Appl. Supercond.* **26**(7), 0611305 (2016).
- ²⁸G. Mörré, J. Sjölund, and M. Leijon, "A review of permanent magnet models used for designing electrical machines," *IEEE Trans. Magn.* **58**(11), 2102719 (2022).
- ²⁹Y. Henry, S. Mangin, J. Cucchiara, J. A. Katine, and E. E. Fullerton, "Distortion of the Stoner–Wohlfarth astroid by a spin-polarized current," *Phys. Rev. B* **79**, 214422 (2009).
- ³⁰E. Oniciuc, L. Stoleriu, and A. Stancu, "LLB simulation of the temperature dependent switching critical curve of a Stoner–Wohlfarth macrospin in the presence," *J. Magn. Magn. Mater.* **352**, 99 (2014).
- ³¹H. ElBidweihy, "Rotational magnetization lag-angle plots using the anisotropic Stoner–Wohlfarth model," *IEEE Trans. Magn.* **53**(11), 7300906 (2017).
- ³²N. A. Zarkevich, C. I. Nlebedim, and R. W. McCallum, "Parameterization of the Stoner–Wohlfarth model of magnetic hysteresis," *J. Magn. Magn. Mater.* **530**, 167913 (2021).
- ³³C. A. Iglesias, J. C. R. de Araújo, E. F. Silva, M. Gamino, M. A. Correa, and F. Bohn, "Fundamental inequalities in the Stoner–Wohlfarth model," *Phys. Rev. B* **106**, 094405 (2022).
- ³⁴I. Petrilă and A. Stancu, "Hysteresis characteristics of an analytical vector hysteron," *Physica B* **406**, 906 (2011).
- ³⁵W. Xu, N. Duan, S. Wang, Y. Guo, and J. Zhu, "Modeling and measurement of magnetic hysteresis of soft magnetic composite materials under different magnetizations," *IEEE Trans. Ind. Electron.* **64**(3), 2459 (2017).
- ³⁶N. C. Pop, "A model for magnetic hysteresis," *Eur. Phys. J. Plus* **134**, 567 (2019).
- ³⁷A. Papoulis, *Probability, Random Variables, and Stochastic Processes* (McGraw-Hill, 1984).
- ³⁸C. Appino and F. Fiorillo, "A model for the reversible magnetization in amorphous alloys," *J. Appl. Phys.* **76**(9), 5371 (1994).
- ³⁹D. Rodríguez-Sotelo, M. A. Rodríguez-Licea, I. Araujo-Vargas, J. Prado-Olivarez, A.-I. Barranco-Gutiérrez, and F. J. Perez-Pinal, "Power losses models for magnetic cores: A review," *Micromachines* **13**, 418 (2022).
- ⁴⁰C. Appino, "Representation of memory in particle assembly hysteresis models," *IEEE Trans. Magn.* **45**(11), 5184 (2009).